Monthly Notices
of the
ROYAL ASTRONOMICAL SOCIETY

MNRAS **454,** 1453–1467 (2015) doi:10.1093/mnras/stv2039

Estimating the impact of the Galactic bar on the evolution of Galactic star clusters from *N*-body simulations

L. J. Rossi★ and J. R. Hurley

Centre for Astrophysics and Supercomputing, Swinburne University of Technology, Hawthorn, VIC 3122, Australia

Accepted 2015 August 28. Received 2015 August 24; in original form 2015 August 4

ABSTRACT

We present an analysis of the effect of a barred gravitational potential on the evolution of several properties of star clusters, constructing a model of the Galactic bar and evolving a set of direct *N*-body simulations of star clusters within the resulting potential. As a first step, we have confirmed that the Galactic bar has a negligible effect on the evolution of star clusters orbiting at distances of 4 kpc or greater from the Galactic Centre. We then performed an extensive orbital analysis in order to identify typical families of planar orbits in the inner regions of a Milky Way-like barred bulge, and followed the evolution of several structural parameters of clusters belonging to the four main orbit families that were identified. We have shown that the orbit type can strongly influence the evolution of total mass, size, core radius, internal velocity dispersion and escape rates of the simulated clusters. Mass-loss rate and dissolution time of the clusters are found to be sensitive to the tidal forcing along the different orbits. We describe a method to predict dissolution times and mass-loss rates of clusters evolving within a barred potential, following any orbit and with any initial mass. Finally, we applied our method to predict the dissolution time and to reconstruct the initial mass of two Galactic bulge clusters with known orbits, namely NGC 6553 and HP 1.

Key words: methods: numerical – Galaxy: bulge – globular clusters: general – Galaxy: structure.

1 INTRODUCTION

The evolution of star clusters is dominated by several processes, which can be grouped into two main categories: internal and external. Internal processes include stellar evolution and two-body relaxation. External processes are linked to the interaction with the galactic environment and include adiabatic tidal disruption, bulge/disc shocks and dynamical friction. Previous studies (Baumgardt & Makino 2003; Gieles et al. 2006; Gieles, Athanassoula & Portegies Zwart 2007; Hurley & Bekki 2008; Lamers, Baumgardt & Gieles 2010; Küpper et al. 2010; Kruijssen et al. 2011; Gieles, Heggie & Zhao 2011; Renaud, Gieles & Boily 2011; Berentzen & Athanassoula 2012; Rieder et al. 2013; Renaud & Gieles 2015a,b, amongst others) showed that the tidal forcing that the clusters experience along their trajectory in the galaxy has a strong influence on their dynamical evolution. A sophisticated modelling of the external tidal field is then particularly important when describing the evolution of globular cluster systems, where the clusters form and evolve in different regions of their host galaxy.

The effect of a sophisticated description of several non-axisymmetric components of the galactic tidal field on the evolution of star clusters by using *N*-body simulations has been investigated in previous works. As an example, Gieles et al. (2006) studied the encounters between giant molecular clouds and star clusters and how they affect the clusters' mass-loss rates and dissolution times. In a subsequent work, Gieles et al. (2007) analysed the effect of spiral patterns in the disc of a galaxy on the evolution of star clusters following planar orbits. In this study, we will present an analysis of the effect of a refined description of the Galactic bulge on the evolution of star clusters. We will refer to the 'bulge' as to the (almost spherically) component of the Milky Way, covering the region out to about 4 kpc from the Galactic Centre. More specifically, we will implement a model of a central rotating bar in NBODY6 (Aarseth 2003), a state-of-the-art code to simulate in great detail the evolution of stellar clusters. The addition of a time-dependent potential such as that generated by a rotating bar represents an improvement with respect to the public version of the code. In fact, the present-day version of NBODY6 includes a description of the gravitational potential generated by a disc-like galaxy, where the bulge is modelled simplistically as a point mass, and hence unresolved. The literature is rich with studies estimating the impact of a central rotating bar on Galactic trajectories of Galactic globular clusters (e.g. Pichardo, Martos & Moreno 2004; Allen, Moreno & Pichardo 2006, 2008; Moreno, Allen & Pichardo 2008; Moreno, Pichardo & Velázquez 2014). On the other hand, the only previous work devoted to a detailed analysis of clusters evolving within a barred potential using direct *N*-body simulations has been proposed by Berentzen

★ E-mail: lucarossi@swin.edu.au

& Athanassoula (2012). The authors followed the dynamical evolution of clusters and their tidal tails located on planar periodic orbits. They showed that the mass-loss rate of their simulated clusters is mainly determined by the average value of the tidal field experienced by the clusters along the orbit and that the shape of the tidal tails is strongly influenced by the bar. However, their simulated star clusters were composed of equal-mass particles and they introduced a gravitational softening length in the force calculation. As crucial improvements, in this work we introduce more input physics such as a particle mass function, stellar evolution, formation of binaries, multiple systems and collisions between stars. In fact, two-body relaxation plays a major role in the internal evolution of a star cluster, being a collisional system (Heggie & Hut 2003), inducing effects such as star escape and mass segregation. Removing the gravitational softening length from the modelling is then important in order to obtain more realistic results. We also extend the analysis to non-periodic planar orbits, identified by extensive orbital analysis.

Another problem to address when describing the evolution of systems of star clusters is related to the fact that a direct modelling of massive star clusters is extremely time consuming (Heggie 2014). The computational effort required to simulate entire star cluster systems is well beyond the possibilities offered by the present methods. Several solutions have been proposed to overcome this problem (e.g. Vesperini & Heggie 1997; Baumgardt & Makino 2003; Gieles et al. 2006, 2007; Lamers et al. 2010). In these studies, the mass-loss rates and the dissolution times of clusters in tidal fields following different orbits and with different initial masses and density profiles have been computed in terms of analytical equations calibrated by using the results of *N*-body simulations. Following this approach, in our previous work (Rossi & Hurley 2015) we proposed a semi-analytic evolutionary model calibrated to simulations of small-*N* clusters to predict the dissolution time and the mass evolution of star clusters in relation to their orbits within the host galaxy. However, that model is only valid for the simplistic case of an axisymmetric representation of the host galaxy. In the present work, we extend the method to the more general case of time-dependent potentials, such as that generated by a rotating bar.

The paper is structured as follows. In Section 2, we present the model of the Galactic bar and our set of *N*-body simulations. Section 3 includes an analysis of the effect of the bar on some of the main parameters defining a star cluster, an orbital analysis performed in order to identify typical orbit families in a barred potential and a study of how different trajectories influence the dynamical evolution of the simulated clusters. In Section 4, we follow the evolution of the tidal radius of the clusters in comparison to the theoretical predictions. Section 5 presents our new evolutionary model based on small *N*-body simulations to describe the mass evolution of clusters in time-dependent tidal fields and in Section 6 we discuss the results of our analysis.

2 METHODS

2.1 Model of the Galaxy

The current public version of NBODY6 (Aarseth 2003) includes a description of the gravitational potential generated by a multicomponent disc galaxy composed of a bulge, disc and halo. In particular, the bulge is described as a point mass, the disc is represented by a classic Miyamoto–Nagai potential (Miyamoto & Nagai 1975) and the halo is modelled as a logarithmic potential. We refer to Rossi & Hurley (2015, hereafter Paper I) for a more comprehensive summary of the potential implemented in NBODY6. We now extend the description of the gravitational potential by adding a central rotating bar, modelled as a triaxial ellipsoid following a Ferrers density profile (Pfenniger 1984)

$$\rho(x,y,z) = \begin{cases} \rho_c(1-m^2)^n, & m < 1 \\ 0, & m \geq 1 \end{cases}, \quad (1)$$

where n is a positive integer and

$$m^2 = \frac{x^2}{a^2} + \frac{y^2}{b^2} + \frac{z^2}{c^2}.$$

In this notation a, b and c are the semi-axes of the ellipsoid, where $a > b > c$. According to previous studies adopting a Ferrers ellipsoid to model the Galactic bar (e.g. Pfenniger 1984; Ortolani et al. 2011; Berentzen & Athanassoula 2012), we set the density profile parameter $n = 2$. As seen in projection on the Galactic plane from the North Galactic Pole, the Galactic bar rotates in a clockwise direction with pattern speed $\Omega_{\rm bar}$. We refer to Appendix A and to Pfenniger (1984) for a detailed characterization of the gravitational potential and forces associated with this mass distribution. Hereafter, we will refer to the version of NBODY6 including a more sophisticated description of the Galactic bulge as NBODY6+BAR. The adopted values of the parameters of the Galactic mass model and the associated references are summarized in Table 1. Fig. 1 shows the mass density on the Galactic plane as a function of the Galactocentric distance (top panel) and the logarithmic colour map of the mass density projected on the (x, z) plane (bottom panel). Both of the plots show the mass density along the major axis a of the Galactic bar. The corotation resonance for the adopted mass model is located at approximately 4.2 kpc from the Galactic Centre.

We note that the total mass of the model is the same as in Paper I, but in this work 98 per cent of the bulge mass is included within the bar, while only 2 per cent is included in the point-mass component (not included in Fig. 1).

In order to compare the evolution of star clusters in a barred potential with the more simplistic case of an axisymmetric potential, it is useful to define an axisymmetrized version of the barred mass model. We will refer to the axisymmetrized version as the model that includes the whole mass of the bulge within the point-mass component (in other words, the same mass model adopted in Paper I). It is important to note that this approach involves two steps: first making the potential axisymmetric and then

Table 1. Parameters of the adopted mass model. In this notation, $M_{\rm b,tot}$ is the total mass of the bulge. $M_{\rm bar}$ is the mass of the bar, a, b and c are the semi-axes of the bar, $\Omega_{\rm bar}$ is the pattern speed of the bar and n defines mass density profile of the bar. $M_{\rm disc}$ is the total mass of the disc, $a_{\rm disc}$ and $b_{\rm disc}$ are scalelengths defining the Miyamoto–Nagai potential. $R_\odot$ is the assumed Galactocentric distance of the Sun and $v_{\rm LSR}$ is the value of circular velocity curve at $R_\odot$.

Parameters	Value	Reference
$M_{\rm b,tot}$	1.0×10^{10} M$_\odot$	Irrgang et al. (2013)
$M_{\rm bar}$	9.8×10^{9} M$_\odot$	Weiner & Sellwood (1999)
a	3.5 kpc	Gardner & Flynn (2010)
b	1.4 kpc	
c	1.0 kpc	
$\Omega_{\rm bar}$	55.9 km s^{-1} kpc	
n	2	Pfenniger (1984)
$M_{\rm disc}$	7.2×10^{10} M$_\odot$	Irrgang et al. (2013)
$a_{\rm disc}$	3.26 kpc	
$b_{\rm disc}$	0.29 kpc	
$R_\odot$	8.33 kpc	Gillessen et al. (2009)
$v_{\rm LSR}$	239.7 km s^{-1}	Irrgang et al. (2013)

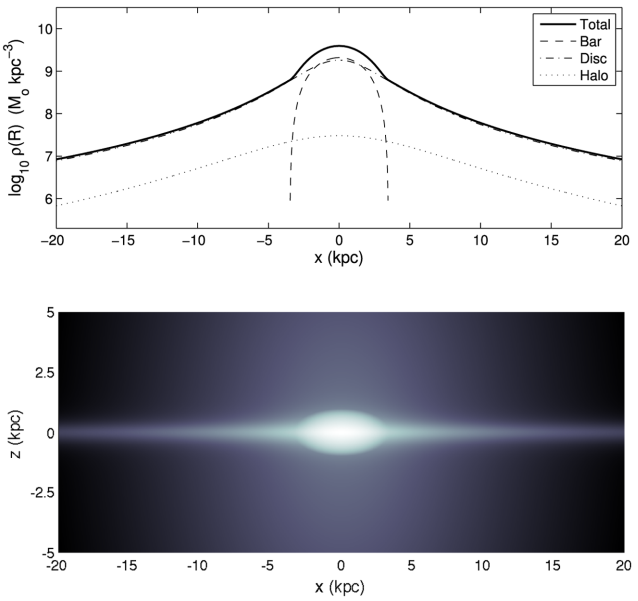

Figure 1. Top panel: mass density on the Galactic plane as a function of the x coordinate, along the bar semimajor axis. The different lines indicate the contribution of the various Galactic components, as indicated in the legend. Bottom panel: logarithmic colour map of the mass density projected on the (x, z) plane. The plots do not include the contribution of the central point mass, since the density would be infinite and hence not graphically representable.

changing the radial density profile in the inner regions. However, about 70 per cent of the total mass of the bar is included within only 1.5 kpc from the Galactic Centre, so we expect the axisymmetry breaking to be the dominant effect for Galactocentric distances greater than this value.

To address some of the problems posed by our analysis we used NIGO (Rossi 2015), a Numerical Integrator of Galactic Orbits. This standalone code has proved to be a useful support to NBODY6 for a wide range of experiments, such as preliminary orbital analysis, calibration of mass models and numerical orbit integration accuracy tests. NIGO includes an implementation of the gravitational potential model implemented in NBODY6+BAR and can simulate the orbit of a large number of test particles, allowing us to predict the Galactic orbits of star clusters returned from NBODY6. We note that in NIGO the star cluster is represented as one test particle and the integration of an orbit is much faster than a full N-body integration. Furthermore, the integration of the equations of motion (EoMs) in NIGO is performed with a Shampine–Gordon integration scheme, while NBODY6 is based on the Hermite integration scheme. The consistency of the orbits predicted from the two codes acts as further proof of the validity of the methods that we adopted (see Appendix A).

2.2 Initial set-up of the simulations

Consistent with Paper I, our simulated star clusters are characterized by a Kroupa stellar initial mass function (Kroupa 2001). The stars follow a Plummer sphere distribution (Plummer 1911) and are initially in virial equilibrium. We did not take the tides into account in the virial equilibrium calculation, i.e. we neglected any dependence of the Plummer models on the initial position and velocity of the clusters in the Galaxy. For all the simulations, we selected the value of the metallicity to be [Fe/H] $= -0.5$. The fraction of primordial binaries has been set equal to 5 per cent of the initial number of stars and the binary orbital set-up has been chosen as described in Geller, Hurley & Mathieu (2013). In our N-body simulations, we chose an approximate initial value of the escape radius of our star cluster, doubling the value determined by applying equation (A6) of Paper I to the axisymmetrixed version of our mass model

$$r_{\rm lim}^3 = \frac{GM_{\rm c}}{\frac{1}{R}\frac{{\rm d}\Phi(R)}{{\rm d}R}\Big| - \frac{{\rm d}^2\Phi(R)}{{\rm d}R^2}\Big|_{R_{\rm c}}} \quad . \tag{2}$$

We refer to Paper I for a description of the various terms in the equation. The choice to double the value of the escaper radius is dictated by the fact that equation (A6) is valid in the case of circular orbits in axisymmetric potentials. An underestimation of the maximum distance after which a star is treated as an escaper in the simulation may cause an exclusion of stars still gravitationally bound to the cluster, resulting in a misinterpretation of the evolution of the cluster parameters. Setting this limit to a value which should be comfortably larger than the actual tidal radius avoids this effect, noting that there is no harm in continuing to integrate stars after they ceased to be bound. In fact, the only motivation for invoking an escape radius during the simulations is to save computational effort by reducing N over time as stars are deemed to have escaped.

3 DYNAMICS OF STAR CLUSTERS IN A BARRED POTENTIAL

3.1 The 'radius of influence' of the bar

The first piece of information that we need in order to characterize the dynamics of a star cluster under the influence of a non-axisymmetric bulge is the minimum distance from the Galactic Centre at which we can confidently neglect the impact of a bar on the evolution of the clusters. In order to obtain an indication of the effect of the bar as a function of the Galactocentric distance of the clusters, we ran a set of N-body simulations of star clusters following different trajectories. In particular, we followed the evolution of clusters orbiting in the Galactic plane initially located at $R = 1$, 2, 3, 4, 6 and 8 kpc with initial number of stars $N = 1 \times 10^4$, 2×10^4 and 5×10^4. The initial velocity of the clusters is the one generating a circular orbit in the axisymmetrized mass model. Since we know the dissolution time for these clusters in the axisymmetrized potential (see Paper I), we can compare the dissolution time expected for the clusters within an axisymmetric potential and the dissolution time from the new set of models. We also note that a clockwise and an anti-clockwise orbital evolution of a cluster in an axisymmetric potential are equivalent. On the other hand, initial state vectors with the same magnitude but opposite direction of rotation will result in different orbits when the potential includes a rotating bar and, in principle, we expect that different trajectories will affect the evolution of star clusters in different ways. Following these considerations, in this experiment we studied separately the cases of orbits rotating in the same direction and in the opposite direction with respect to the Galactic bar. As seen from the North Galactic Pole, the bar rotates in a clockwise direction and the angular momentum vector points towards the South Galactic Pole. We then will refer to clockwise and anti-clockwise rotating trajectories as orbits with aligned and anti-aligned angular momentum with respect to the angular momentum of the bar, respectively.

For all the simulations, we defined the time of dissolution as the time at which only 300 stars remain gravitationally bound. The reason for this choice is to avoid small-N statistical fluctuations in the dissolution time due to the presence of hard binaries (or not),

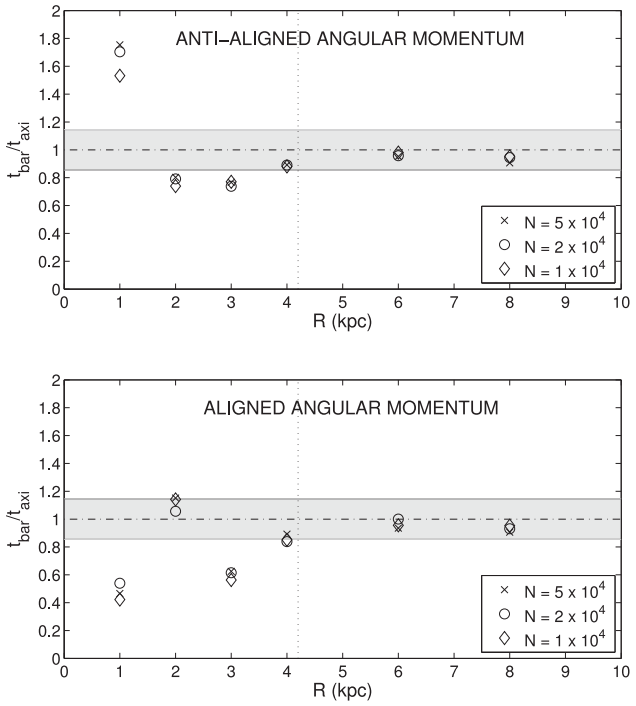

Figure 2. Ratio of the dissolution time of clusters evolving in a barred potential and of the predicted dissolution time if the clusters were evolving in an axisymmetric potential. The vertical dotted lines show the location of the corotation resonance. The shaded area represents the uncertainties affecting the value of the theoretical dissolution time. Such uncertainties have been computed by propagating the errors on the values of the parameters β and k (see equation 3) derived in Paper I.

which could overly affect the evolution of the final stages of a star cluster.

In order to evaluate the extent of the dynamical influence of the bar, for each N-body simulation we computed the ratio of the dissolution time in a barred potential to the dissolution time predicted by equation (13) of Paper I, valid to describe clusters following circular planar trajectories in the axisymmetrized mass model. We recall that

$$t_{\rm diss} = k \left[\frac{N}{\ln(\gamma N)}\right]^{\beta} \left[\frac{1}{R}\frac{{\rm d}\Phi(R)}{{\rm d}R} - \frac{{\rm d}^2\Phi(R)}{{\rm d}R^2}\right]^{-1/2} , \qquad (3)$$

where $\gamma = 0.02$, $\beta = 0.88$, $k = 256.53$, R is the Galactocentric distance of the cluster's centroid, Φ is the Galactic gravitational potential and N is the initial number of stars. Fig. 2 shows the results of this analysis.

First, we note that simulated clusters with different initial number of stars show the same value of the ratio of dissolution times within the uncertainties on the theoretical value of the dissolution time (the importance of this result will be discussed in Section 5). The ratio between the dissolution time in an axisymmetric potential and the dissolution time in a barred potential converges to unity, within the uncertainties of the theoretical model, for Galactocentric distances greater than 4 kpc, while its value fluctuates in the inner regions of the Galaxy. As expected, orbits with aligned and anti-aligned angular momentum with respect to the angular momentum of the bar show different values of the ratio of the dissolution times. The inclusion of a bar leads to a change of the shape of the clusters' trajectories, which then experience different tidal forcing along their orbits, inducing changes in the mass-loss rates and hence in the dissolution times. The change of the orbit's shape is more important for clusters with aligned orbital angular momentum, as is noticeable in the bigger fluctuations of the ratio between dissolution times in Fig. 2. Quite surprisingly, we found that the cluster on the innermost orbit with anti-aligned angular momentum survives longer than the cluster with same initial conditions moving in an axisymmetric potential. Such a difference could be owing to the different radial mass density profile in the very inner regions of the Galaxy, as described above. In the light of these preliminary results, in this work we have focused our subsequent analysis on the inner 4 kpc of the Galaxy, which corresponds roughly to the radius of the corotation resonance. Furthermore, simulations with a barred potential are computationally more challenging than those without a bar, since the EoMs associated to a bar are quite complicated (see Appendix A). This provides further justification for taking into account the presence of a Galactic bar only where it is needed.

3.1.1 *Orbits of the star clusters, bar shocks and mass-loss rates*

Lamers et al. (2010) studied the effect of orbital eccentricity on the mass-loss rate of clusters in a steady tidal field. The authors concluded that the mass-loss rate varies with the orbital period of the cluster and it is found to be higher at the perigalactic passage of the cluster. In this section, we analyse the evolution of the mass-loss rates of clusters orbiting within the inner regions of a barred Milky Way-like bulge. The mass-loss is studied after the initial phase of evolution, which is dominated by stellar evolution effects. As test cases, we selected two clusters from our sample, namely the clusters initially located on the Galactic plane at 1 and at 2 kpc, respectively, and with orbital angular momentum aligned with the angular momentum of the bar. Both the clusters are initially composed of $N = 2 \times 10^4$ stars. We then evaluated the evolution of the mass-loss rate for the two cases during two orbital periods in the bar-corotating frame of reference. Fig. 3 shows the result of our analysis. Focusing first on the cluster located initially at 1 kpc (left-hand column of Fig. 3), we note that the maxima in the mass-loss rate (or equivalently, the minima of ${\rm d}M/{\rm d}t$) are not strictly related to the perigalactic passages of the cluster. Instead, it appears that the mass-loss rate decreases in correspondence with the first two perigalactic passages and it is enhanced at the apogalactic passages. On the other hand, the third (and easily largest) drop in the derivative is clearly related to a close perigalactic passage. Similar behaviour is found for the cluster initially located at 2 kpc. The first perigalactic passage corresponds to an enhancement in the mass-loss rate, whereas the second and third spikes in mass-loss correspond to the apogalacticon of the clusters and the second perigalactic passage is associated with a minimum of the mass-loss rate (a maximum of the derivative). Delving deeper, we found a correlation between the minima of ${\rm d}M/{\rm d}t$ and the maxima of the curvature of the orbit (lower panels in Fig. 3). This could be expected, since the maxima in the curvature of the orbit correspond to a sudden deceleration and subsequent acceleration of the cluster, leading to a quick variation of the magnitude and direction of the velocity vector. In other words, the mass-loss rate peaks in correspondence with the maxima of the centrifugal acceleration experienced by the cluster in the bar-corotating frame of reference. However, in-line with the results of Lamers et al. (2010), close perigalactic passages can still lead to increases in the mass-loss rate, as noticeable during the third perigalactic passage of the cluster initially located at 1 kpc. There is also evidence for the mass-loss rate pattern to have a frequency related to the orbital period of the clusters in the bar-corotating frame of reference rather than to the

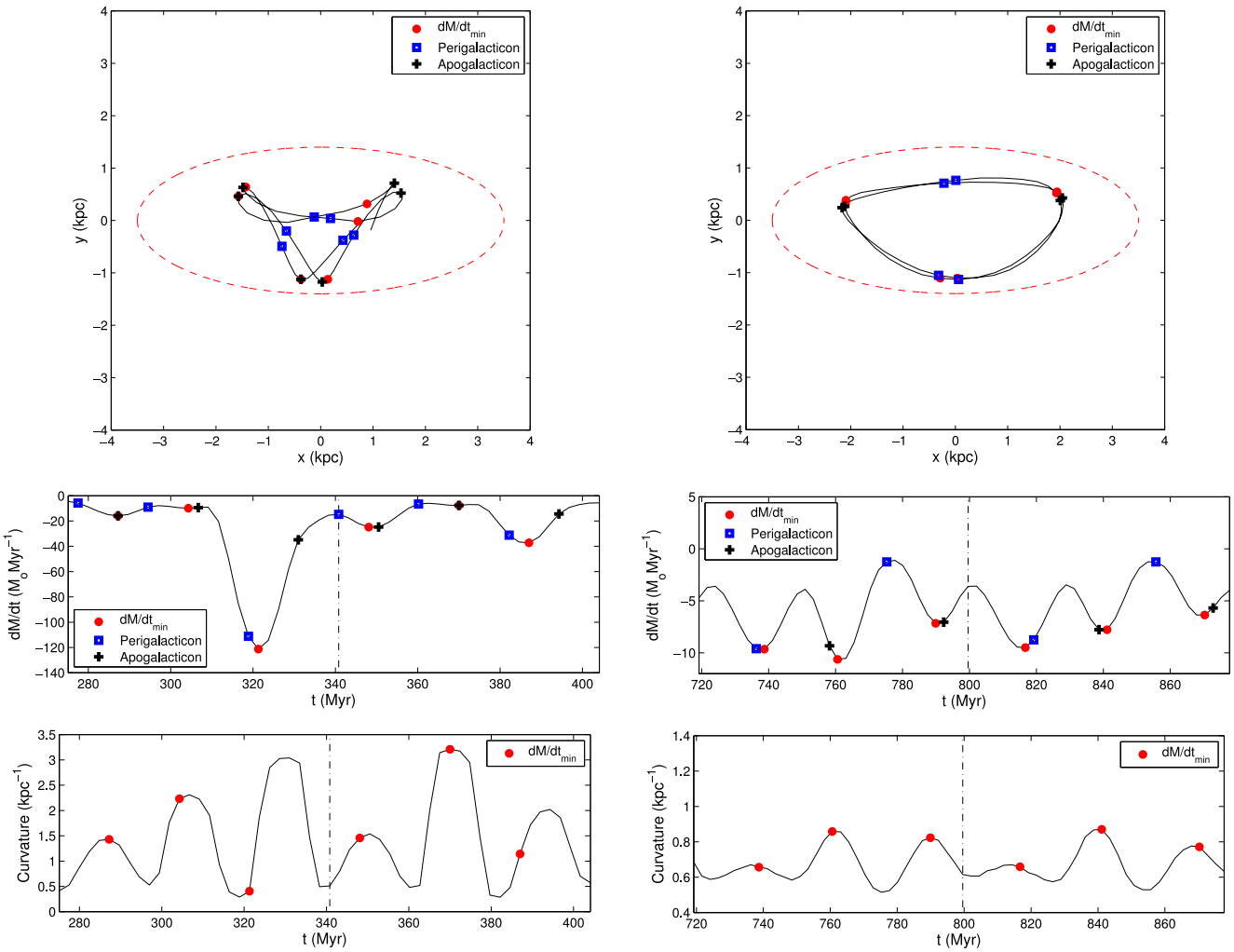

Figure 3. Top panels: projection of the orbit on the Galactic plane as seen in the bar-corotating frame of reference for the star clusters with $N = 2 \times 10^4$ and with bar-aligned angular momentum, initially located at 1 kpc (left-hand panel) and 2 kpc (right-hand panel). The initial velocity of the clusters is the one generating a circular orbit in the axisymmetric gravitational potential. The red dashed line shows the contours of the bar. The orbits are shown for two orbital periods. Middle panels: time evolution (for two orbital periods) of the first time derivative of the total number of stars for the cluster initially located at 1 kpc (left-hand panel) and 2 kpc (right-hand panel). Bottom panels: time evolution (for two orbital periods) of the curvature of the orbit of the clusters for the cluster initially located at 1 kpc (left-hand panel) and 2 kpc (right-hand panel). In all the plots, the red filled circles indicate the moment of the minimum in the number-loss rates, the open blue squares the moment of the perigalactic passages and the black crosses the moment of the apogalactic passages. The vertical black dot–dashed lines show the separation between the two orbital periods considered.

orbital period in the inertial frame. Finally, we note that there is a time delay between the increase in the mass-loss clearly induced by a close perigalactic passages and the perigalactic passage itself (see the third perigalactic passage of the cluster starting at 1 kpc in the left-hand column of Fig. 3). This evidence is consistent with the results of Küpper et al. (2010).

3.1.2 Effect of the bar on some fundamental structural parameters of a star cluster

As a preliminary analysis of the effect of the bar on the evolution a star cluster, we compared the evolution of some of the structural parameters of a star cluster in the case of an axisymmetric and a barred potential. Fig. 4 shows the evolution of total mass, half-mass radius and internal velocity dispersion of two clusters with $N = 10^5$ stars evolving in the axisymmetrized mass model and in the barred mass model, respectively. Both clusters have same initial position on the Galactic plane ($R = 3$ kpc) and same initial velocity vector. The value of the initial velocity is the one generating a circular orbit in the axisymmetrized mass model. First, we note that in this case the cluster evolving in the barred potential dissolves more quickly than the cluster in the axisymmetric potential. After an initial mass-loss phase dominated by stellar evolution processes, in which the evolution of the two clusters is similar, the cluster on the barred potential experiences a higher mass-loss rate than the one in the axisymmetric potential. Also, the sizes of the two clusters are different. Even though the overall trend of the half-mass radius is similar for the two cases, the cluster on the circular orbit in the axisymmetric tidal field grows larger than the one in the barred model. The evolution of the internal velocity dispersion of the cluster members shows the same trend in both cases, but for the simulation with the bar the cluster experiences some kicks in the velocity dispersion, corresponding to the moment of the perigalactic passages and/or to the maxima in the centrifugal acceleration in the

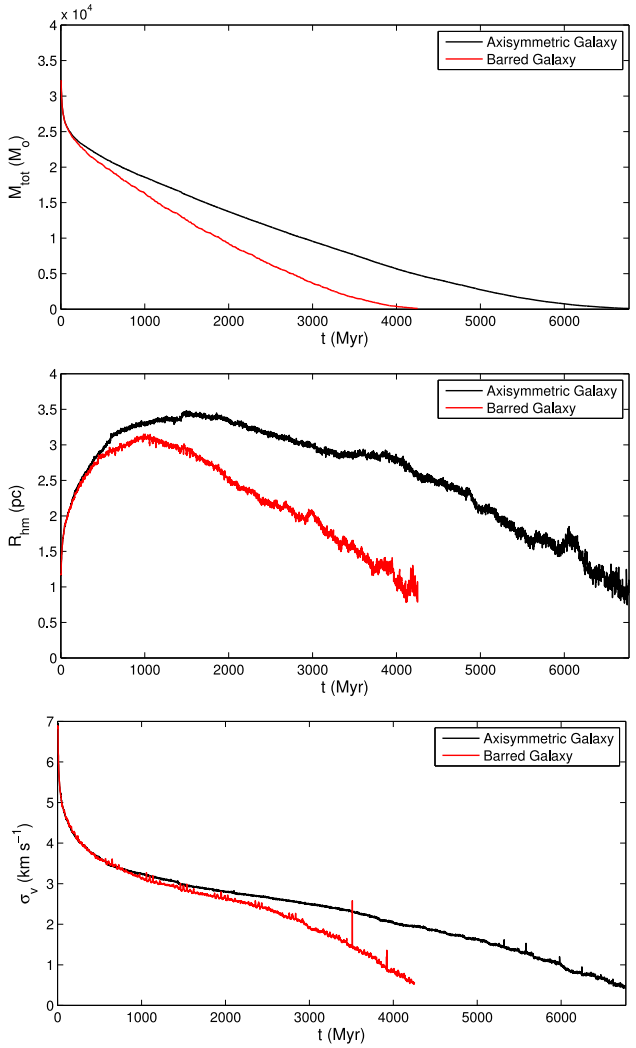

Figure 4. Effect of a Galactic bar on the evolution of total mass, half-mass radius and internal velocity dispersion of two initially identical clusters with $N = 10^5$ stars evolving within an axisymmetric potential and a rotating-barred potential, respectively.

bar-corotating frame of reference, as discussed above. On the other hand, the cluster on the circular orbit presents a more regular trend.

3.2 Orbital analysis

In Section 3.1, we showed that, according to the results of our simulations, the presence of a bar has a non-negligible effect on the dissolution time of clusters in the inner 4 kpc of the Galaxy. We also noted that different initial conditions generate different orbits with different dissolution times.

Now we face the problem of characterizing the dependence of the evolution of clusters on their trajectory in the Galaxy. The only previous work that presented *N*-body simulations of star clusters in a barred potential (Berentzen & Athanassoula 2012) is focused on the study of clusters on periodic orbits in the frame of reference corotating with the bar. According to the authors of that study, the importance of these orbits resides in the fact that they are the backbones of stellar bars, because they can confine regular regions in phase space around them. In order to present a more complete study, we performed an orbital analysis to identify typical families of planar orbits in a barred potential.

The main tool that we used is the classic Poincaré surface section (or Poincaré diagram). We present an analysis similar to the one proposed in Pichardo et al. (2004), in which the authors showed different Poincaré surface sections generated by different models of the Galactic bar. We briefly recall that the presence of an integral (or constant) of motion in a dynamical system reflects the presence of symmetries, according to Noether's theorem (for a brief review see Heggie & Hut 2003, p. 59). In particular, in an axisyimmetric static potential the conservation of energy corresponds to the time symmetry of the system, while the conservation of the *i*–component of the angular momentum reflects the symmetry of the system along the *i*-axis. For the case of a rotating-barred potential, both these symmetries are broken and neither the energy nor the angular momentum are conserved singularly, but a combination of them is. The new integral of motion is the Jacobi's constant E_j, which in the rotating frame of reference has the form (Binney & Tremaine 2008)

$$E_\mathrm{j} = \frac{1}{2}|\dot{\boldsymbol{x}}|^2 + \Phi - \frac{1}{2}|\boldsymbol{\Omega} \times \boldsymbol{x}|^2, \tag{4}$$

where $(\boldsymbol{x},\dot{\boldsymbol{x}})$ are position and velocity in the corotating frame of reference, respectively, Φ is the specific potential energy and $\boldsymbol{\Omega}$ is the pattern speed of the bar. We created the Poincaré surface section following the usual procedure. For each orbit, and in the bar-corotating frame of reference, we found the crossing points x_c of the orbit of the test particles with the x-axis and the corresponding velocity component $v_{x,\mathrm{c}}$. Corresponding to each intersection, we plotted a point $(x_\mathrm{p}, v_{x,\mathrm{p}})$ in the Poincaré diagram, where

$$\begin{cases} x_\mathrm{p} = x_\mathrm{c} \\ v_{x,\mathrm{p}} = v_{x,\mathrm{c}} \end{cases} \quad \text{if } v_{y,\mathrm{c}} > 0$$
$$\begin{cases} x_\mathrm{p} = -x_\mathrm{c} \\ v_{x,\mathrm{p}} = -v_{x,\mathrm{c}} \end{cases} \quad \text{if } v_{y,\mathrm{c}} < 0\ . \tag{5}$$

The main advantage of the surface section for orbital analysis studies is that two orbits with the same energy cannot occupy the same point of the Poincaré diagram. In our specific case of a barred potential, the Jacobi integral is the equivalent of the energy and the orbital analysis was performed in the bar-corotating frame of reference.

The next step is to select a typical value of the Jacobi integral for bulge star clusters and to create the associated Poincaré diagram. To do this, we took the sample of eight Galactic bulge globular clusters with known state vectors (generated assuming a Galactocentric distance of the Sun equal to $R_\odot = 8.3$ kpc) found in Rossi et al. (2015). Fig. 5 shows the Jacobi integral of the selected sample of star clusters, obtained by combining their initial state vector with the adopted Galactic model. The dispersion of the value of E_j within the sample bulge clusters is relatively small and in this study we selected as the typical E_j the mean value $\langle E_\mathrm{j}\rangle = -2.1274 \times 10^{-5}$ $(\mathrm{km\ s^{-1}})^2$.

Next we generated a set of initial conditions for test particles in the inner 4 kpc of the Galaxy with the selected $\langle E_\mathrm{j}\rangle$ value for the Jacobi integral and integrated their orbits in the gravitational potential described in Section 2.1. We generated the Poincaré diagram by integrating 100 orbits forward in time for 4000 Myr using NIGO (Rossi 2015). The Poincaré section is shown in Fig. 6.

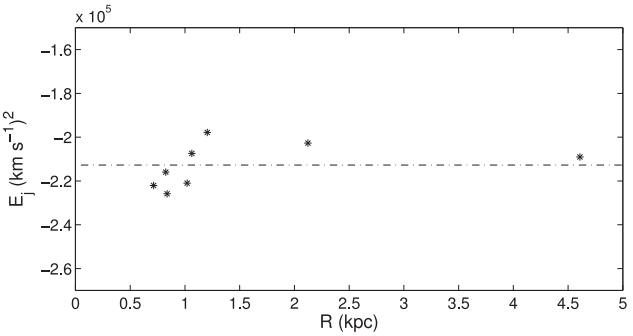

Figure 5. Jacobi integral for eight bulge globular clusters with known state vector as a function of their Galactocentric distance. The dot–dashed line represents the average value of E_j.

Inspired by the results of Pichardo et al. (2004), we identified four main families of orbits, which have been highlighted with different colours in Fig. 6. A more detailed description of each orbit family is presented in Section 3.3. In order to estimate how different orbits, and hence different tidal forces, influence the evolution of star clusters in the inner regions of a Milky-Way-like galaxy, we chose a representative orbit for each family and ran *N*-body simulations of clusters following the selected trajectories.

3.3 Evolution of clusters belonging to different orbital families

In this section, we present the evolution of clusters belonging to the identified orbit families. For each orbit family, we selected a representative orbit and followed the evolution of a cluster with initial number of stars $N = 5 \times 10^4$ until dissolution. We note here that, even though the simulated star clusters are not as massive as the more massive globular clusters that we observe in the Galaxy, results from small-number simulations can be used to retrieve information on bigger clusters, as discussed in Section 5.

3.3.1 Family I

The clusters belonging to Family I follow a boxy trajectory in the bar-corotating frame of reference. Their orbital angular momentum is aligned with the angular momentum of the bar and the minimum value of the perigalactic distance that the clusters reach is approximately equal to the semiminor axis of the bar ($b = 1.5$ kpc). The blue lines in the plots of Fig. 7 show the evolution of some of the main parameters characterizing the evolution of a cluster with initial $N = 5 \times 10^4$ stars. In order to compare the behaviour of different cluster families, we plotted the evolution of the parameters as a function of the time normalized to the dissolution time. The star cluster does not experience dramatic mass-loss events along its trajectory, and the overall trend of the mass evolution is quite smooth. However, it

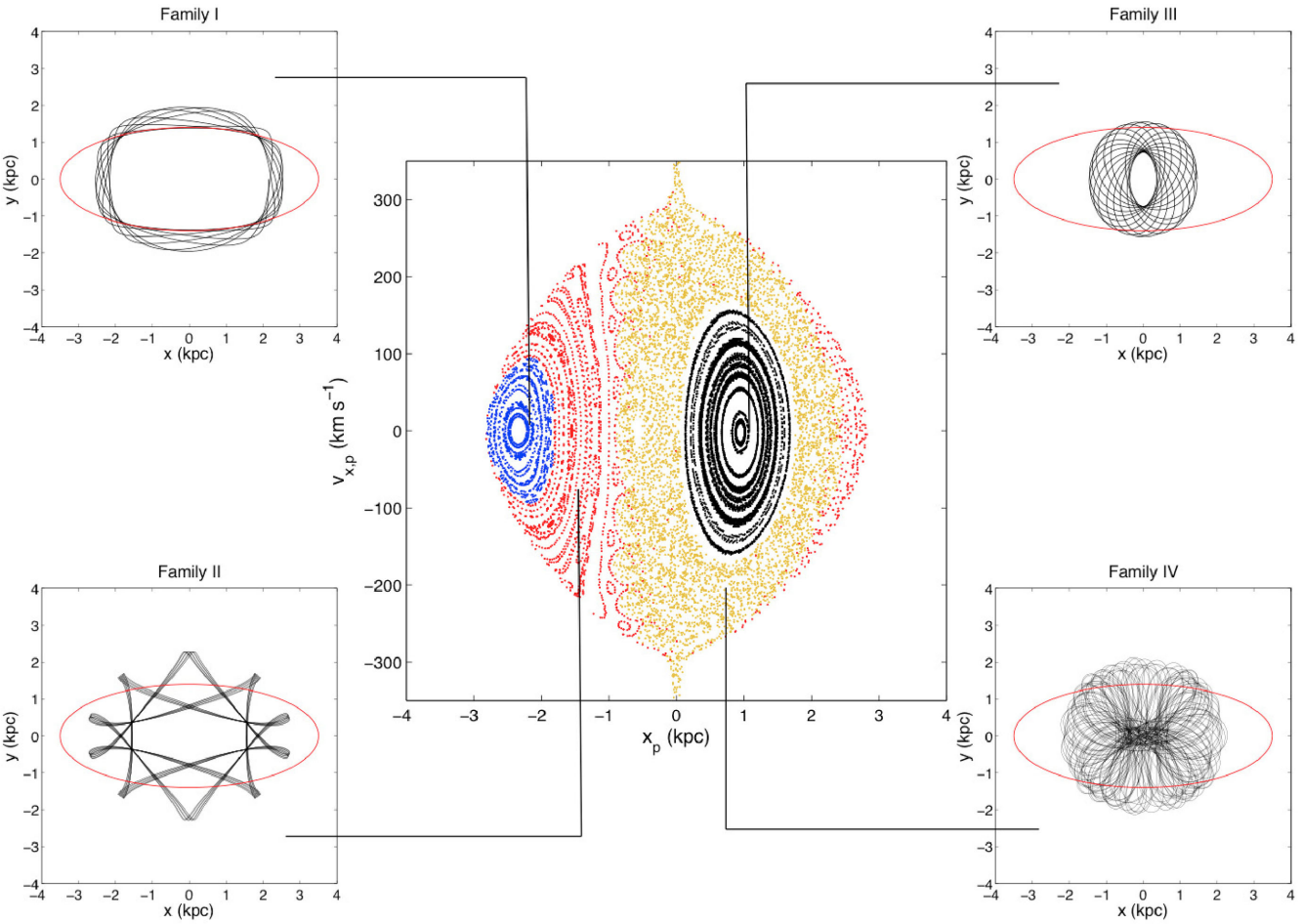

Figure 6. Poincaré diagram and identified families of orbits generated by integrating the equation of motion of 100 test particles in the adopted mass model. The corresponding value of the Jacobi integral is $\langle E_j \rangle = -2.1274 \times 10^{-5}$ (km s^{-1})^2. Four distinct orbit families are identified and a typical orbit highlighted for each (with the bar ellipsoid shown in red for reference).

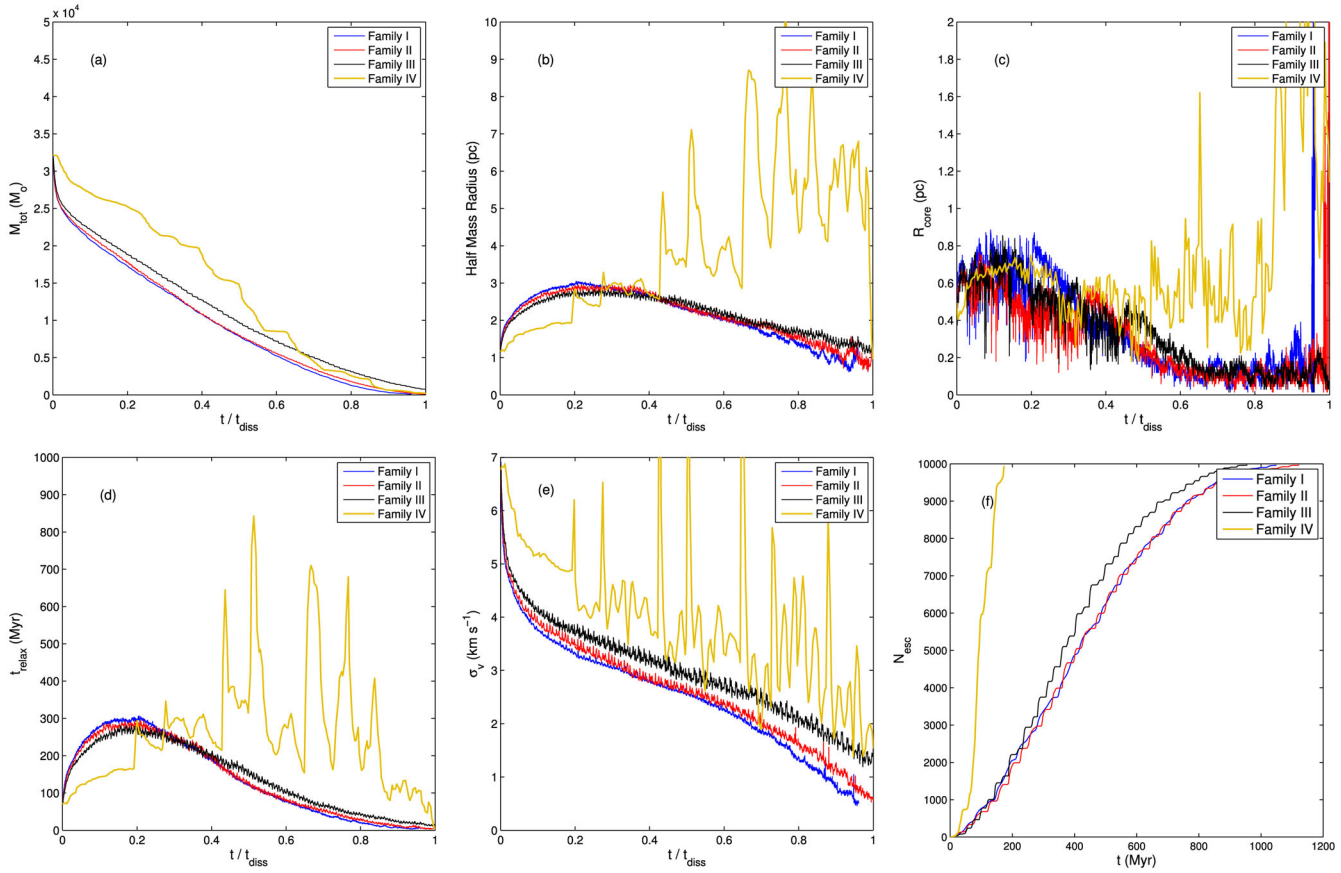

Figure 7. Evolution of some of the fundamental parameters of the simulated star clusters. Panels (a)–(e) show the results for simulations with initial $N = 5 \times 10^4$ stars, while panel (f) shows the results for simulations with initial $N = 1 \times 10^4$ stars. The blue, red, black and yellow lines show the results for clusters belonging to the orbital Families I, II, III and IV, respectively. Panel (a): evolution of the total mass normalized to the dissolution time. Panel (b): evolution of the half-mass radius normalized to the dissolution time. Panel (c): evolution of the core radius normalized to the dissolution time. Panel (d): evolution of the half-mass relaxation time normalized to the dissolution time. Panel (e): evolution of the velocity dispersion of the cluster members normalized to the dissolution time. Panel (f): evolution of the cumulative number of escapers until dissolution. The reason for which this plot the results of simulations with $N = 1 \times 10^4$ stars instead of $N = 5 \times 10^4$ stars is that for small N runs the effect of the bar shocks on the total number of escapers can be visualized easily than for bigger N runs.

is evident that bar shocks have some minor effects on the cluster. In particular, we note that the velocity dispersion of the cluster members experiences some kicks (Fig. 7e), which relates to an increase in the cumulative number of the escapers (Fig. 7f).

3.3.2 *Family II*

The star clusters belonging to Family II change the direction of rotation with respect to the bar rotation (in the bar-corotating frame of reference), as indicated by the distribution of the red points in Fig. 6. The clusters are confined within the bar for most of their orbital period and their trajectory is elongated along the bar semi-major axis. Also in this case, the simulated star cluster ($N = 5 \times 10^4$ stars) experiences mild shocks along its orbit, which induce a small modulation in the mass-loss trend (Fig. 7c), a kick in the velocity dispersion of the cluster members (Fig. 7e) and an increase in the cumulative number of escapers (Fig. 7f). Also, the evolution of the half-mass radius presents a typical trend found in other works (e.g. Sippel et al. 2012), and the core collapse of the simulated star cluster happens at about 2/3 of the cluster lifetime (see Fig. 7c). The simulated star cluster dissolves after about 4200 Myr of evolution. We note that the evolution of the cluster belonging to this orbital family resembles very closely the evolution of the cluster belonging to Family I, and also the dissolution times are comparable. This could be explained as a consequence of the same average tidal forces experienced by the clusters, as evident from the similarity between the orbits of Families I and II.

3.3.3 *Family III*

The orbits belonging to Family III anti-rotate with respect to the bar and they are confined within the bar for most of their orbital period. In the bar-corotating frame of reference, these orbits are elongated along the semiminor axis of the bar. The perigalactic passages of this orbital family are closer to the Galactic Centre than Families I and II, and the clusters survive for a shorter time as a consequence of the stronger tidal field. This effect is visible in Fig. 7(f), where the cumulative number of escapers of the cluster belonging to Family III presents a steeper gradient than Families I and II. However, as for the Family I and Family II orbits, the overall evolution of the cluster mass is quite regular, with small increases in the velocity dispersion of the cluster members induced by bar shocks. Also in this case, the core collapse happens at about 2/3 of the cluster's lifetime. The dissolution time in this case is about 3200 Myr.

3.3.4 Family IV

The orbits of Family IV are characterized by chaotic behaviour (yellow points in Fig. 6). They frequently change the direction of rotation with respect to the rotation of the bar during their orbital evolution, they are mostly confined within the bar and can reach very small perigalactic distances. Of all of the families that we identified, this family is the one that affects in the most dramatic way the evolution of a star cluster that follows one of its orbits. We followed the evolution of a star cluster with initial number of stars $N = 5 \times 10^4$ and plotted the results in Fig. 7. When the cluster reaches its perigalactic distance all its structural parameters experience a strong perturbation. The evolution of total mass, half-mass radius, velocity dispersion and cumulative number of escapers indicates that the internal evolution of the cluster is strongly affected by the tidal shocks. The extreme perturbation due to tidal shocks is easily visible in the evolution of the velocity dispersion of the cluster members (Fig. 7e), where the energy gain from the gravitational interaction with the external field at the perigalactic passage induces sudden kicks and consequent relaxation in the σ_v profile. This simulated cluster with $N = 5 \times 10^4$ stars dissolves in about 340 Myr, i.e. a much shorter lifetime than Families I–III.

We also evaluated the relative importance of each family of orbits in populating the Poincaré diagram. The results show that 20 per cent of the orbits belong to Family I, 28 per cent belong to Family II, 26 per cent belong to Family III and 26 per cent belong to Family IV. Considering that the initial position and velocity of the clusters with same Jacobi integral have been selected randomly, it appears that each orbit family has roughly the same probability of realization in the adopted mass model.

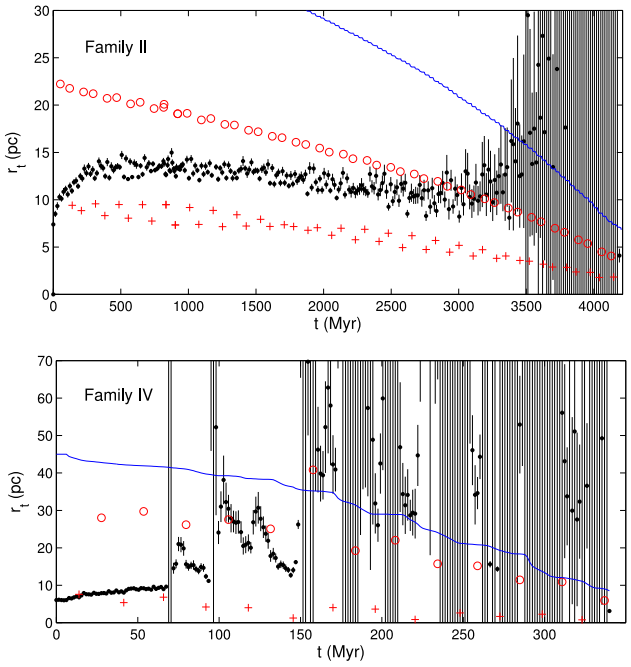

Figure 8. Evolution of the tidal radius of the simulated star clusters. The black points represent the tidal limit and the associated uncertainties obtained by fitting a King profile to the clusters. The red open circles and crosses represent the tidal limit at the apogalactic passage and perigalactic passage, respectively, obtained from equation (6). The continuous blue line shows the boundary imposed in the simulations in order to identify escapers.

4 EVOLUTION OF THE TIDAL RADIUS

In previous work (e.g. Allen et al. 2006, 2008; Moreno et al. 2014), the tidal limit of star clusters in a barred potential has been determined using the theoretical value given by

$$r_t = \left[\frac{GM_c}{\left(\frac{\partial F_r}{\partial r}\right) + \dot{\theta}^2 + \dot{\phi}^2 \sin^2\theta} \right]^{1/3}, \quad (6)$$

where M_c is the mass of the star cluster and F_r is the component of the gravitational acceleration along the line that connects the cluster centre with the Galactic Centre. (r,θ,ϕ) are the spherical coordinates of the cluster in the inertial Galactocentric frame of reference. We refer to Allen et al. (2006) for a detailed derivation of equation (6), which represents a generalization for a 3D orbit in a generic tidal field of equation (A6) in Paper I, which in turn is valid for the simplistic case of a cluster on a circular planar orbit within an axisymmetric potential. In this section, we aim to check whether the tidal radius of our simulated clusters evolving within a barred potential is consistent with the prediction given by equation (6).

We fitted a King profile (King 1962)

$$\Sigma(r) = K \left\{ \frac{1}{\left[1 + (r/r_c)^2\right]^{1/2}} - \frac{1}{\left[1 + \left(r_{t,k}/r_c\right)^2\right]^{1/2}} \right\}^2 \quad (7)$$

to our simulated star clusters along their trajectory, where $\Sigma(r)$ is the surface density as function of the distance from the cluster centre, K is a scale constant, r_c is a core radius and $r_{t,k}$ is the tidal radius. We note that in this case we assumed that the tidal limit of the star cluster corresponds to the point where its surface density drops to zero. An alternative method (Webb et al. 2013) is to evaluate the distance from the centre of the cluster of the farthest gravitationally bound star, which can be determined according to the value of the energy of the cluster members. We then compared the fitted tidal radius of the cluster along its orbit with the maximum tidal limit (at the apogalactic passage) and the minimum tidal limit (at the perigalactic passage) computed from equation (6). Fig. 8 shows the results for the clusters with initial $N = 5 \times 10^4$ stars, belonging to the identified orbit Families II and IV. We note that the evolution of the tidal radius for Families I and III is not shown because these are qualitatively similar to that of Family II. For the tidal limit obtained by fitting a King profile to the simulated star cluster, we also included the uncertainty calculated using a non-linear least-squares fit method.

The clusters in orbit Families I–III show similar behaviour. At the start of the simulation the tidal radius of the star clusters is approximately the theoretical tidal radius at the perigalactic passage. They start to expand until eventually they reach their maximum size, after which their tidal radius decreases as a consequence of mass loss. Towards the final stages of the cluster's evolution, the fit with a King profile is less robust than in the initial phases, as seen in the increase of the error bars associated to the fitted tidal limit. For the clusters belonging to Families I–III, we can conclude that, considering the uncertainties of the fit model, the tidal limit obtained by fitting the distributions of the stars in the clusters with a King profile is included within the maximum and the minimum tidal limit predicted by equation (6). This result can be explained considering that a 'tidal radius' of a King profile is not directly related to the tides, but merely describes the size of the cluster. When going from perigalactic to apogalactic, the actual tidal radius grows (see e.g. Webb et al. 2013), but the growth of the King radius, which is set by relaxation, takes longer. The differences between the theoretical and the fitted tidal limits can

then be interpreted in terms of the delayed response of the cluster to the external tidal field. On the other hand, the fit fails miserably for the cluster belonging to Family IV. We recall that this star cluster experiences important bar shocks, which strongly perturb its whole structure. Immediately after the third perigalactic passage the fit produces a jump in the tidal limit from about 10 to 20 pc. After this shock, the tidal limit eventually decreases until the next perigalactic passage, when the cluster experiences another strong perturbation. This behaviour repeats until the sixth perigalactic passage, after which the cluster cannot relax to an equilibrium configuration.

In Fig. 8, we have also shown the maximum distance from the cluster centre that defines the limit of the clusters in the *N*-body simulations (as described in Section 2.2). Its value is about as twice as big as the maximum value of the theoretical tidal limit at the apogalactic passage, confirming that that we are not excluding any of the cluster members in the *N*-body simulation.

5 A NEW FORMULATION OF THE EVOLUTIONARY EQUATIONS

In Paper I, we proposed an evolutionary model calibrated to the results of a set of *N*-body simulations of star clusters evolving in an axisymmetric potential and following eccentric orbits slightly inclined to the Galactic plane. As we noted in Section 3.1, the model we proposed in Paper I still represents a good analytical description of the evolution of disc clusters orbiting in a barred Galaxy at Galactocentric distances $R \gtrsim 4$ kpc, where the presence of the bar has a negligible impact on the evolution of star clusters. The scenario in the inner regions of the Galaxy is more complicated. In fact, we found that when a bar is present the Galactic orbit of a star cluster influences its evolution in a non-trivial way. Also, slightly different initial conditions generate orbits belonging to different families, that show sensible differences in their dynamical evolution. It seems then a hard task to calibrate a trivial equation that predicts the dissolution time as function of the Galactic orbit of a cluster in the bulge. A possible solution of the problem of modelling the mass-loss processes of star clusters in complex potentials can be found in Kruijssen et al. (2011). The authors modelled the mass-loss rates due to stellar evolution and dynamical evolution using an approach based on detailed stellar evolution models and semi-analytic descriptions of two-body relaxation and tidal shocks.

In this section, we propose an alternative method to predict the lifetime and the mass-loss evolution of a star cluster with any initial mass on any Galactic orbit based on the results of direct *N*-body simulations. According to our solution, all we need is an *N*-body simulation of the cluster on the selected orbit with an initial arbitrary number of stars. We recall equation (3) which describes the dissolution time of a cluster on a circular orbit in the Galactic plane. We can separate the equation into two components: the first term in parenthesis described the dependence of the dissolution time of the star cluster on internal dynamical processes, while the second term in parenthesis describes the dependence of the dissolution time on the tidal interaction of the cluster with the external potential. The theoretical ratio between the dissolution time of two clusters on the same orbit with initial number of stars N_1 and N_2 is

$$\frac{t_{\rm diss}(N_1)}{t_{\rm diss}(N_2)} = \left[\frac{N_1 \ln(\gamma N_2)}{N_2 \ln(\gamma N_1)}\right]^x , \qquad (8)$$

where the dependence of the external potential disappears as a common factor in the equation. We can use the results of *N*-body simulations presented in Paper I (for $N = 1 \times 10^4$, 2×10^4, 3×10^4 and 4×10^4) and the new set of simulations with a barred potential to check whether equation (8) can predict the ratio between dissolution times to good accuracy. In the top panel of Fig. 9 we show the ratio between the dissolution time for a cluster following a circular trajectory in an axisymmetric potential for the simulation set presented in Paper I compared to the theoretical prediction given by equation (8). The *R*-axis value of the data points corresponds to the initial Galactocentric distance of the cluster. The bottom panel of Fig. 9 shows the results of the same analysis applied to the simulation set of clusters evolving in a barred potential presented in the this work. For each initial Galactocentric distance, we plotted both the ratio for orbits with aligned and anti-aligned orbital angular momentum. The results show that equation (8) can predict to good accuracy the ratio between dissolution times of clusters with different initial masses following the same Galactic orbit for both the simulations in the axisymmetric potential and in the barred potential. We note that generally the best results are obtained when comparing the dissolution times of clusters with initial number of stars $N \gtrsim 2 \times 10^4$. An interpretation of this behaviour could be that the simulations with initial number lower than this limit are affected by statistical noise to a greater degree. However, we also note that the value of $t_{\rm diss}(40{\rm k})/t_{\rm diss}(10{\rm k})$ for the cluster at 1 kpc in the axisymmetric model determined from the *N*-body simulations deviated significantly from the theoretical prediction. Such a discrepancy could be owing to a combination of a small-number effect and of the fact that the cluster with $N = 1 \times 10^4$ stars orbiting at 1 kpc dissolves quickly (in about 184 Myr).

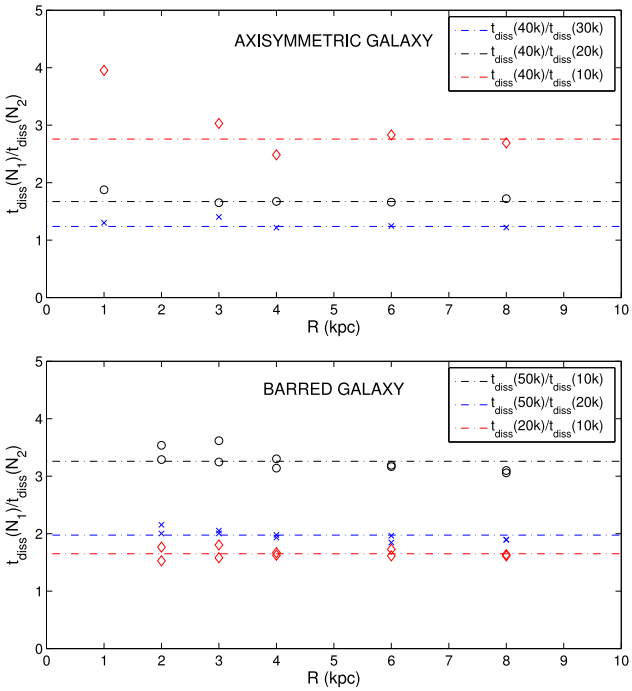

Figure 9. Ratio between dissolution times of star clusters with different initial number of stars and following the same orbit. The ratio between dissolution times is plotted as function of the initial Galactocentric distance of the clusters. The dash–dotted lines show the theoretical prediction for different initial numbers, as indicated in the legend of the figures. The open circles, diamonds and crosses show the results from *N*-body simulations. The results for clusters evolving in an axisymmetric mass model are shown in the top panel, while in the bottom panel presents the results for a barred Galactic model.

At this point, we advance the hypothesis that the mass evolution of star clusters on the same orbit scales with the dissolution time and with the initial mass of the cluster. We assume that we can describe the mass evolution of a cluster with initial mass $M_1(0)$ on a certain orbit by using a certain function of the time

$$M_1(t) = f_1(t). \tag{9}$$

Our hypothesis is that a second cluster on the same orbit with initial mass $M_2(0)$ experiences a mass loss described by

$$M_2(t) = f_2(t), \tag{10}$$

where

$$f_2(t) = \frac{M_2(0)}{M_1(0)} f_1\left(\frac{t}{C}\right) \tag{11}$$

and

$$C = \left[\frac{N_2 \ln(\gamma N_1)}{N_1 \ln(\gamma N_2)}\right]^{\beta}. \tag{12}$$

This assumption can be justified by the results shown in Fig. 7. In fact, for the orbital Families I–III the evolution of the clusters' parameters is only mildly affected by bar shocks, and the overall mass loss follows a quite regular trend. Furthermore, we noticed that the ratio of dissolution times of clusters in an axisymmetric and in a barred mass model (see Fig. 9) presents the same behaviour for clusters with different initial masses, suggesting the presence of a scale relation between dissolution times of clusters with different masses on the same orbit. In order to test the validity of our hypothesis, we performed the following test. We consider a cluster following the representative orbit of Family III. We ran simulations of this star cluster using different initial number of stars, in particular $N = 1 \times 10^4$, 2×10^4, 5×10^4 and 1×10^5 stars. We then fitted the mass evolution of the cluster with $N = 2 \times 10^4$ with the power-law form proposed in Paper I

$$M_{20k}(t) = M_{20k}(0)\left[1 - \left(\frac{t}{t_{diss}(20k)}\right)^{\alpha}\right], \tag{13}$$

where $t_{diss}(20k)$ is the dissolution time of the cluster resulting from the simulation. Following our method, we have all the information required to predict the mass evolution of a cluster with any initial number of stars on the selected orbit. We then compared our theoretical prediction with the results of the N-body simulations with $N = 1 \times 10^4, 5 \times 10^4$ and 1×10^5 stars. Fig. 10 shows the results of this experiment. We note that also in this case the predicted dissolution times are consistent with the results of the N-body simulations and that the mass-loss trends are reproduced well. In particular, the main difference between the simulation result and our prediction is accentuated in the initial phase of the clusters' evolution, where the mass loss by stellar evolution plays a major role.

The next step is to check whether this result holds for different orbits, as we expect. We ran two simulations ($N = 2 \times 10^4$ and 5×10^4 stars) for each of the four orbit families that we identified. We then fitted a power-law mass evolution to the simulations with $N = 2 \times 10^4$ stars and compared the theoretical prediction with the results of the $N = 5 \times 10^4$ N-body simulations. The results are shown in Fig. 11. The predicted mass evolution is consistent with the output of the simulations. We also note that each orbit family is characterized by a slightly different value of the slope α. The values of the slope parameter of the mass-loss function obtained for the various orbit families are $\alpha_{\rm I} = 0.52$, $\alpha_{\rm II} = 0.49$, $\alpha_{\rm III} = 0.56$ and $\alpha_{\rm IV} = 0.97$. This is likely a consequence of the differences in the tidal forces experienced by the clusters on different orbits,

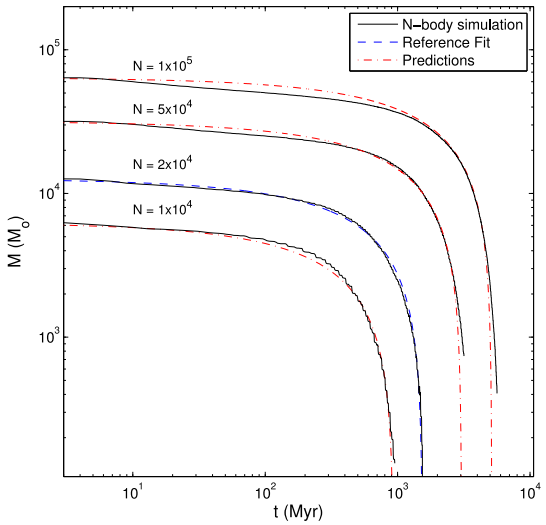

Figure 10. Mass evolution of a set of simulations of star clusters belonging to Family III. The continuous black lines represent the results of $N = 1 \times 10^4$, 2×10^4, 5×10^4 and 1×10^5 N-body simulations. The dashed blue line is the fitted power-law mass evolution to the cluster with $N = 2 \times 10^4$ stars, while the dot–dashed red lines represent the prediction from our theoretical model for the other valued of N.

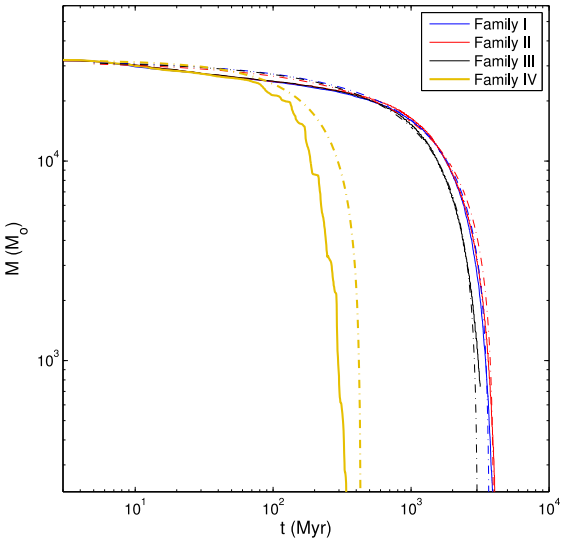

Figure 11. Comparison between the mass evolution of star clusters with initial number of stars $N = 5 \times 10^4$ from N-body simulations and the prediction obtained applying our theoretical model using simulations with a lower number of stars ($N = 2 \times 10^4$).

which result in different average mass-loss rates. Fig. 11 shows also that in the case of a cluster on a chaotic orbit (Family IV), where importantly the mass-loss events owing to tidal shocks dominate the mass evolution of the clusters, the derived scaling relations predict the mass evolution to a lower degree of accuracy than for more regular orbits.

For the non-chaotic orbits, we can conclude that the scaling relations derived in Paper I, valid for clusters evolving within an axisymmetric potential, also apply to the case of a barred potential.

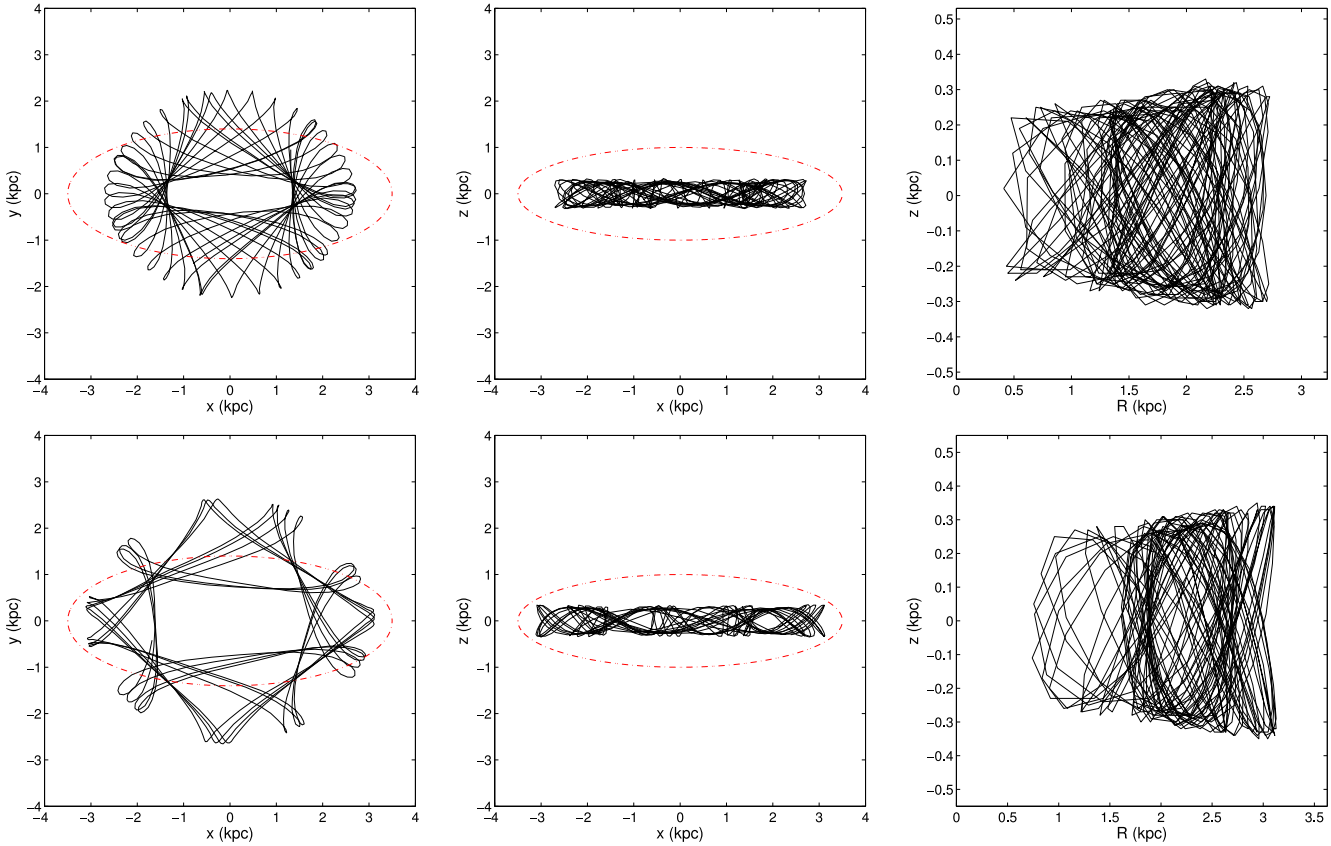

Figure 12. Projection of the Galactic orbit of HP 1 (top three panels) and of NGC 6553 (bottom three panels) on the Galactic plane (left-hand panel), on the (x, z) plane (central panel) and on the meridional plane (right-hand panel). Each orbit is shown in the bar-corotating frame of reference. The dot–dashed red line shows the contours of the bar.

5.1 Reconstructing the initial mass of the globular clusters HP 1 and NGC 6553

As an example application, we applied this evolutionary model to reconstruct the mass-loss history of HP 1 and NGC 6553, two globular clusters ∼13.7 and ∼13 Gyr old, respectively, located in the Galactic bulge and with an initial state vector determined by Ortolani et al. (2011) and Zoccali et al. (2001). We determined the current mass of the clusters from the value of their absolute V magnitude listed in the Harris catalogue (Harris 1996, 2010 version). Form the magnitude, we obtained the luminosity and then the mass by applying the liner mass-to-light ratio from Bonatto & Bica (2012). For further details we refer to Paper I. The mass obtained for HP 1 and NGC 6553 are $M_{\rm HP1} = 1.63 \times 10^4$ and $M_{\rm NGC6553} = 7.1194 \times 10^4\,{\rm M}_\odot$, respectively. The simulated clusters with initial number of stars $N_2 = 2 \times 10^4$ with the same orbits of HP 1 and NGC 6553 and followed the evolution of the clusters until dissolution. We also note that in this case the trajectory of the clusters is not confined within the Galactic plane, but has a 3D shape. In order to check whether the derived scaling relations are valid also for the case of orbits slightly inclined to the Galactic plane we performed additional test N–body simulations, finding positive results. Fig. 12 shows the projection of the orbit of HP 1 and of NGC 6553 on the Galactic plane (x, y), on the (x, z) plane (in the bar-corotating frame of reference) and on the meridional plane (R, z), where $R = (x^2 + y^2)^{1/2}$. Interestingly, the projection of the orbits of both clusters on the Galactic plane belongs to our identified orbital Family II. We set the initial phase angle of the bar equal to 25°, which is similar to the value estimated for the Galactic bar according to Pichardo et al. (2004). We then fitted a power-law mass-loss function to the results of the simulations to determine the best value of the slope α and solved the evolutionary equation for the star cluster applying the Newton–Raphson method, similarly to what we have done in Paper I. More specifically, in this case to find the initial mass $M_1(0)$ of the target globular cluster corresponds to finding the zero value of the equation

$$M_1(0) + c_1 M_1(0)^{1-c_2} (\ln c_3 M_1(0))^{c_2} + c_4 = 0 \quad , \tag{14}$$

where

$$\begin{cases} c_1 = -\left(\frac{t}{t_{\rm diss}(N_2)}\right)^{\alpha} \left(\frac{M_2}{\ln(\gamma A M_2)}\right)^{\alpha\beta} \\ c_2 = \alpha\beta \\ c_3 = \gamma A \\ c_4 = -M_1(t) \end{cases} . \tag{15}$$

In this notation $M_1(t)$ is the present-day mass of the target globular cluster and A is the scaling factor to convert between initial mass and initial number of stars of the cluster under the assumption of a Kroupa initial stellar mass function ($N = AM$). Fig. 13 shows the reconstructed mass-loss history of HP 1 using the results of the simulation. According to our result, the initial mass of HP 1 was $M_{\rm HP1}(0) \sim 2.45 \times 10^5\,{\rm M}_\odot$ and its dissolution time is $t_{\rm diss,\,HP1} \sim 15.6$ Gyr. For NGC 6553, our approach predicts an initial mass of $M_{\rm N6553}(0) \sim 3.39 \times 10^5\,{\rm M}_\odot$ and its dissolution time is $t_{\rm diss,N6553} \sim 20.3$ Gyr.

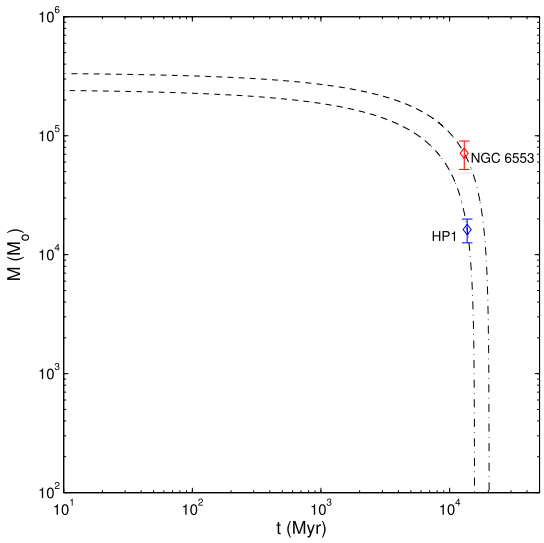

Figure 13. Reconstructed mass-loss history of HP 1 and NGC 6553 obtained by applying the proposed method. The present-day age and mass of HP 1 and NGC 6553 are represented by a blue and red diamond, respectively.

This alternative approach in principle would allow us to reconstruct the mass-loss history of every Galactic globular cluster with known age, present-day mass and orbit once we have calibrated an evolutionary model from a small-number *N*-body simulation of each cluster. We estimate that, taking advantage of the computing power offered by the gSTAR supercomputer at Swinburne University of Technology, we will be able to obtain all the information to predict the mass evolution of a whole Milky Way-like star cluster system within the time frame of a month. The main limitation of this method is that in principle the ratio between dissolution times is valid under the assumption that the tidal field does not change in time. The Galaxy represents a complex evolving environment, and the validity of our method should be tested in time-evolving gravitational potentials. We note that in recent work Renaud & Gieles (2015b) found that the properties of present-day star clusters differ very little, whether the clusters are embedded in a growing galactic halo for 12 Gyr, or in a static one. However, this result does not apply in the context of the bar. Observations and cosmological simulations (Kraljic, Bournaud & Martig 2012, and references therein) show that bars are short lived in the early Universe ($z \gtrsim 1$). These results are consistent with the estimate of the age of the Milky Way bar, which is suspected to be younger than 6 Gyr (Cole & Weinberg 2002). Even if a bar survives several Gyr, its strength can vary significantly because of multiple effects such as accretion of gas, feedback and fuelling of the central region. The other limitation is that currently we do not know the orbit for every Milky Way globular cluster.

6 DISCUSSION AND CONCLUSIONS

We have presented the results of direct *N*-body simulations of star clusters evolving in the gravitational potential generated by a Milky Way-like galaxy, including a refined description of the Galactic bulge modelled as a triaxial, non-homogeneous rotating ellipsoid (a bar). We have found that the bar has a non-negligible effect on the dissolution time and on the mass-loss of clusters located in the inner 4 kpc from the Galactic Centre. This means that to model the evolution of bulge star clusters we have to take into account the presence of the bar, whereas we can confidently neglect it when modelling the evolution of outer-disc star clusters.

As a second step, we performed an orbital analysis in order to identify typical orbit families of star clusters living in the Galactic bulge. We identified four main families of planar orbits, basing our characterization on features of the Poincaré surface section associated to a Jacobi integral representative of observed bulge clusters. More specifically, Family I includes the clusters that rotate in the same direction of the Galactic bar, Family II includes clusters that change direction of rotation with respect to the bar during their orbital evolution, Family III includes bar-anti-rotating orbits and Family IV includes chaotic orbits. We followed the evolution of the main structural parameters of simulated star clusters following an orbit representative of each orbital family. We have found that different orbits influence the mass-loss rates in different way. The overall evolution of the structural parameters of the clusters belonging to Families I–III is quite smooth, with only a small modulation associated to the bar shocks experienced by the clusters along their orbits. The situation is different for clusters belonging to Family IV. For these objects, close perigalactic passages strongly affect the value of all the structural parameters of the star clusters, for which the whole structure experiences a strong perturbation. Also, the dissolution time of these objects is extremely small if compared to the typical age of the observed Milky Way globular clusters. As a conclusion, we might argue that we do not expect to find Galactic clusters on these orbits, because they would have been destroyed in the very early stages of the bar instability development. On the other hand, if we do find such clusters, they could give us important constraints on the age of the Galactic bar. However, care has to be taken when interpreting the results for these clusters. In fact, since their perigalacticon is very close to the Galactic Centre, where the mass density is higher, dynamical friction could play a major role in affecting their orbital and internal evolution only making it more likely for them to have dissolved. Along with dynamical friction, radial migration can be associated with spiral perturbations of the Galactic disc (Sellwood & Binney 2002). Even though the spiral pattern in barred galaxies usually develops outside the bar region, and hence is not affecting the orbits of objects located in the bulge, the long-lived Galactic globular clusters could have experienced radial migration, for instance in the early phases of the Milky Way evolution before the development of the bar instability. In this work, we did not consider this effect. Furthermore, the Galaxy model that we adopted still includes a central point mass, representative of the bulge spherical component. It is possible that the extremely strong perturbations that we have found are the consequence of an interaction with a tidal field that quickly diverges in the inner regions of the Galaxy. This highlights how important it is to obtain a sophisticated representation of the inner Galaxy and accurate initial conditions of the clusters when modelling these objects.

We followed the evolution of one of the most important parameters defining a star cluster, the tidal radius. More specifically we tested if the tidal limit of the simulated star clusters obtained by fitting a classical King profile to the projected surface density is consistent with the theoretical value adopted in previous works. We have found that the fitted tidal limit is consistently included within the range defined by the minimum value (at the perigalactic passage) and the maximum value (at the apogalactic passage) predicted by the theory, but does not experience strong oscillations. This could reflect the fact that the clusters don't respond immediately to the sudden changes of the external tidal field, and their sizes correspond to an orbit-averaged value of the tidal limit. Also in this case, the results are different for the clusters belonging to the orbital

Family IV, for which the fit with the King profile failed. Likely the reason for this behaviour is that the whole structure of the clusters is strongly perturbed by bar shocks at the close perigalactic passages, and they are unable to relax to an equilibrium configuration. We also note that there are alternative definitions of the tidal limit, based on energetic arguments (Webb et al. 2013), and it is possible that different definitions will lead to different results. The question of how to best characterize the tidal radius for general orbits will be explored further in future work.

Following the attempt described in Paper I to reconstruct the initial mass of the clusters, we propose an evolutionary model based on small *N*-body simulations. In this case, the scenario is complicated by the non-trivial relation between the orbit of a cluster in the bulge and its mass-loss rate and dissolution time. However, we have found a scale relation connecting the dissolution times of clusters with different initial masses and following the same Galactic orbit. We have found this relation to be valid for a wide range of different initial masses and different Galactic orbits. The main advantage of our method is that it would be able to predict and to reconstruct the mass-loss history of a cluster on any orbit with any initial mass using the results of a low mass *N*-body simulation of the same cluster. In fact, small *N*-body simulations are fast, while direct *N*-body models of massive star clusters are still out of reach in a reasonable time frame. As an application of our method, we have presented the results for the Galactic bulge globular clusters with known Galactic orbits, HP 1 (Ortolani et al. 2011) and NGC 6553 (Zoccali et al. 2001). Both the clusters belong to the identified orbit Family II. According to our results, we have reconstructed initial masses $M_{\rm HP1}(0) \sim 2.45 \times 10^5$ and $M_{\rm N6553}(0) \sim 3.39 \times 10^5$ $M_\odot$ and we have predicted dissolution times $t_{\rm diss,\,HP1} \sim 15.6$ and $t_{\rm diss,\,N6553} \sim 20.3$ Gyr.

However, this approach is not able to predict the evolution of other cluster parameters, such as the core radius, for which direct modelling is still required. On the other hand, it could be useful if the goal is to study the evolution of the mass function of a whole globular cluster system, where the clusters describe different orbits in different parts of the galaxy. Also, in principle the current approach can be extended to other potentials, e.g. elliptical galaxies, so can be used to model extragalactic GC populations. It still has to be tested to which extent the relations that we have found hold in the more realistic case of a time-dependent evolving gravitational potential.

One of the immediate applications of our method could be to simulate Galactic globular clusters with known age and orbit using small *N*-body simulations and predict initial mass and mass-loss history by applying the scale relations that have been derived in this work. As discussed above, one of the main results of an extensive study of clusters located in the Galactic bulge based on the method proposed in the present work could be an estimate of the age of the Galactic bar. Furthermore, we can simulate clusters with the same metallicities as those observed, producing a more realistic evolutionary model.

As already noted, another strong limitation of the present approach is that the gravitational potential is still described in terms of static potentials. In our model the bar rotates as a rigid body with a certain pattern speed, but the mass and structure of the different Galactic components is set at the start of the simulation and does not evolve in time. Renaud & Gieles (2015a) proposed a method to simulate the dynamics of collisional systems in arbitrary, time-evolving potentials. More flexible approaches such as this would allow us to couple NBODY6 with an *N*-body simulation of galaxies located, in principle, anywhere along the Hubble sequence. In our future work, we aim to extend our analysis to this more general case, which would allow us, for example, to study the effect of an evolving short-lived bar.

ACKNOWLEDGEMENTS

We thank Jeremy Webb for valuable discussion regarding the description of the tidal radius. We thank Florent Renaud for constructive comments that we believe helped to improve the quality of the manuscript. This work was performed on the swinSTAR and gSTAR supercomputers at Swinburne University of Technology funded by Swinburne and the Australian Government's Education Investment Fund. LR acknowledges a CRS scholarship from Swinburne University of Technology.

REFERENCES

Aarseth S. J., 2003, in Sverre J., Aarseth S. J., eds, Gravitational N-Body Simulations. Cambridge Univ. Press, Cambridge, UK, 430 pp
Aarseth S. J., 2003, Gravitational N-Body Simulations
Allen C., Moreno E., Pichardo B., 2006, ApJ, 652, 1150
Allen C., Moreno E., Pichardo B., 2008, ApJ, 674, 237
Baumgardt H., Makino J., 2003, MNRAS, 340, 227
Berentzen I., Athanassoula E., 2012, MNRAS, 419, 3244
Binney J., Tremaine S., 2008, Galactic Dynamics, 2nd edn. Princeton Univ. Press, Princeton
Bonatto C., Bica E., 2012, MNRAS, 423, 1390
Cole A. A., Weinberg M. D., 2002, ApJ, 574, L43
Gardner E., Flynn C., 2010, MNRAS, 405, 545
Geller A. M., Hurley J. R., Mathieu R. D., 2013, AJ, 145, 8
Gieles M., Portegies Zwart S. F., Baumgardt H., Athanassoula E., Lamers H. J. G. L. M., Sipior M., Leenaarts J., 2006, MNRAS, 371, 793
Gieles M., Athanassoula E., Portegies Zwart S. F., 2007, MNRAS, 376, 809
Gieles M., Heggie D. C., Zhao H., 2011, MNRAS, 413, 2509
Gillessen S., Eisenhauer F., Fritz T. K., Bartko H., Dodds-Eden K., Pfuhl O., Ott T., Genzel R., 2009, ApJ, 707, L114
Harris W. E., 1996, AJ, 112, 1487
Heggie D. C., 2014, MNRAS, 445, 3435
Heggie D., Hut P., 2003, The Gravitational Million-Body Problem: A Multidisciplinary Approach to Star Cluster Dynamics. Cambridge Univ. Press, Cambridge, UK, 372 pp
Hurley J. R., Bekki K., 2008, MNRAS, 389, L61
Irrgang A., Wilcox B., Tucker E., Schiefelbein L., 2013, A&A, 549, A137
King I., 1962, AJ, 67, 471
Kraljic K., Bournaud F., Martig M., 2012, ApJ, 757, 60
Kroupa P., 2001, MNRAS, 322, 231
Kruijssen J. M. D., Pelupessy F. I., Lamers H. J. G. L. M., Portegies Zwart S. F., Icke V., 2011, MNRAS, 414, 1339
Küpper A. H. W., Kroupa P., Baumgardt H., Heggie D. C., 2010, MNRAS, 401, 105
Lamers H. J. G. L. M., Baumgardt H., Gieles M., 2010, MNRAS, 409, 305
Miyamoto M., Nagai R., 1975, PASJ, 27, 533
Moreno E., Allen C., Pichardo B. S., 2008, Rev. Mex. Astron. Astrofis., 34, 131
Moreno E., Pichardo B., Velázquez H., 2014, ApJ, 793, 110
Ortolani S., Barbuy B., Momany Y., Saviane I., Bica E., Jilkova L., Salerno G. M., Jungwiert B., 2011, ApJ, 737, 31
Pfenniger D., 1984, A&A, 134, 373
Pichardo B., Martos M., Moreno E., 2004, ApJ, 609, 144
Plummer H. C., 1911, MNRAS, 71, 460
Renaud F., Gieles M., 2015a, MNRAS, 448, 3416
Renaud F., Gieles M., 2015b, MNRAS, 449, 2734

Renaud F., Gieles M., Boily C. M., 2011, MNRAS, 418, 759
Rieder S., Ishiyama T., Langelaan P., Makino J., McMillan S. L. W., Portegies Zwart S., 2013, MNRAS, 436, 3695
Rossi L. J., 2015, Astron. Comput., 12, 11
Rossi L. J., Hurley J. R., 2015, MNRAS, 446, 3389
Rossi L. J., Ortolani S., Barbuy B., Bica E., Bonfanti A., 2015, MNRAS, 450, 3270
Sellwood J. A., Binney J. J., 2002, MNRAS, 336, 785
Sippel A. C., Hurley J. R., Madrid J. P., Harris W. E., 2012, MNRAS, 427, 167
Vesperini E., Heggie D. C., 1997, MNRAS, 289, 898
Webb J. J., Harris W. E., Sills A., Hurley J. R., 2013, ApJ, 764, 124
Weiner B. J., Sellwood J. A., 1999, ApJ, 524, 112
Zoccali M., Renzini A., Ortolani S., Bica E., Barbuy B., 2001, AJ, 121, 2638

APPENDIX A: IMPLEMENTING A BAR IN NBODY6

The equations of motion (EoMs) of a particle moving within a certain mass distribution can be expressed in terms of the partial derivatives of the gravitational potential

$$\begin{cases} \ddot{x} = -\frac{\partial \Phi}{\partial x} \\ \ddot{y} = -\frac{\partial \Phi}{\partial y} \\ \ddot{z} = -\frac{\partial \Phi}{\partial z} \end{cases} . \quad \text{(A1)}$$

Explicitly, the EoMs of a particle moving within the gravitational potential generated by the model of the Galactic bar that we introduced in Section 2.1 are (Pfenniger 1984)

$$\begin{cases} \ddot{x} = & -2Cx[W_{100} - 2y^2W_{110} - 2z^2W_{101} - 2x^2W_{200} \\ & + 2y^2z^2W_{111} + 2x^2y^2W_{210} + 2x^2z^2W_{201} + y^4W_{120} \\ & + z^4W_{102} + x^4W_{300}] = -2Cxf_1(x, y, z) \\ \ddot{y} = & -2Cy[W_{010} - 2x^2W_{110} - 2z^2W_{011} - 2y^2W_{020} \\ & + 2x^2z^2W_{111} + x^4W_{210} + 2y^2z^2W_{021} + 2x^2y^2W_{120} \\ & + z^4W_{012} + y^4W_{030}] = -2Cyf_2(x, y, z) \\ \ddot{z} = & -2Cz[W_{001} - 2x^2W_{101} - 2y^2W_{011} - 2z^2W_{002} \\ & + 2x^2y^2W_{111} + x^4W_{201} + y^4W_{021} + 2y^2z^2W_{012} \\ & + 2x^2z^2W_{102} + z^4W_{003}] = -2Czf_3(x, y, z) \end{cases} \quad \text{(A2)}$$

The coefficients W_ijk are functions of the incomplete elliptic integrals of the first and second kind. The integration of the EoMs of the stars in NBODY6 is performed using the Hermite integration scheme, which requires the explicit form of the first time derivative of the forces (jerk). As a first approximation, when computing the jerk we set to zero the first time derivative of the coefficients. The main justification for this is that the size of a typical globular cluster is 3 orders of magnitude smaller than the radius of its orbit and that the typical time-scale of the dynamical evolution of the members within the cluster (e.g. the crossing time) is typically 1 order of magnitude smaller than the orbital period. This allows us to neglect the variation of the coefficients defining the potential when integrating the EoMs of the cluster members. The explicit first time derivative of the EoMs is

$$\begin{cases} \dot{F}_x = & -2C\{\dot{x}f_1(x, y, z) + x[-4y\dot{y}W_{110} - 4z\dot{z}W_{101} \\ & - 4x\dot{x}W_{200} + 4(y\dot{y}z^2 + y^2z\dot{z})W_{111} + 4(x\dot{x}y^2 \\ & + x^2y\dot{y})W_{210} + 4(x\dot{x}z^2 + x^2z\dot{z})W_{201} \\ & + 4y^3\dot{y}W_{120} + 4z^3\dot{z}W_{102} + 4x^3\dot{x}W_{300}]\} \\ \dot{F}_y = & -2C\{\dot{y}f_2(x, y, z) + y[-4x\dot{x}W_{111} - 4z\dot{z}W_{011} \\ & - 4y\dot{y}W_{020} + 4(x\dot{x}z^2 + x^2z\dot{z})W_{111} + 4(y\dot{y}z^2 \\ & + y^2z\dot{z})W_{021} + 4(x\dot{x}y^2 + x^2y\dot{y})W_{120} \\ & + 4z^3\dot{z}W_{012} + 4y^3\dot{y}W_{030}]\} \\ \dot{F}_z = & -2C\{\dot{z}f_3(x, y, z) + z[-4x\dot{x}W_{101} - 4y\dot{y}W_{011} \\ & - 4z\dot{z}W_{002} + 4(x\dot{x}y^2 + x^2y\dot{y})W_{111} + 4x^3\dot{x}W_{201} \\ & + 4y^3\dot{y}W_{021} + 4(y\dot{y}z^2 + y^2z\dot{z})W_{012} + 4(x\dot{x}z^2 \\ & + x^2z\dot{z})W_{102} + 4z^3\dot{z}W_{003}]\} \end{cases} \quad \text{(A3)}$$

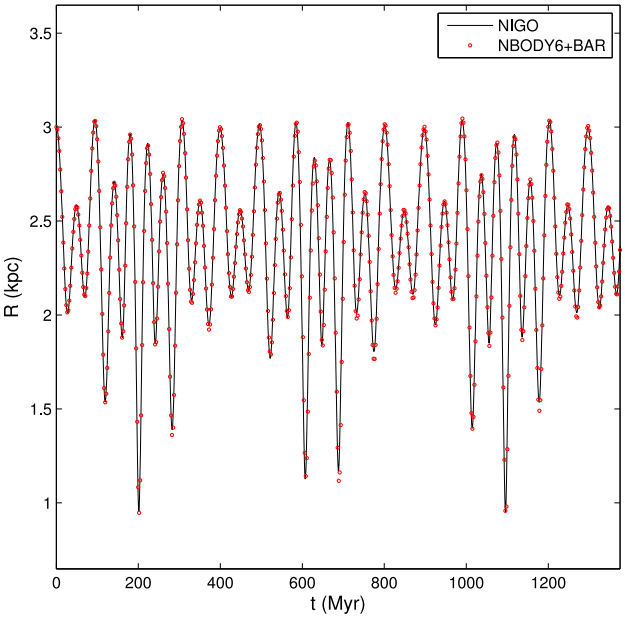

Figure A1. Comparison between the evolution of the Galactocentric distance of a test star cluster predicted by NIGO and by NBODY6+BAR. The Galactic mass model and the initial conditions of the clusters are the same in both cases.

In order to test the reliability of this method, we compared the orbital evolution of a test bulge star cluster predicted by NBODY6+BAR and the trajectory computed with NIGO, assuming the same gravitational potential and initial conditions. We recall that the integration of the EoMs in NIGO is performed with the Shampine–Gordon integration scheme. We are then comparing results from two completely independent methods. Fig. A1 shows the results of this analysis. We note that the evolution of the galactocentric distance of the star cluster is consistent and we can conclude that the approximation of constant W_{ijk} coefficients is valid and NBODY6+BAR can predict orbits in a barred potential to a good approximation.

This paper has been typeset from a TEX/LATEX file prepared by the author.